Predictability of North Pacific blocking events: Analogue-based analysis of historical MIROC6 simulations

Anupama K Xavier, Oisín Hamilton, Davide Faranda, Stéphane Vannitsem

Received: 24 April 2025 | Revised: 26 November 2025 | Accepted: 4 December 2025

DOI: 10.1002/qj.70104

Quarterly Journal of the Royal Meteorological Society RMetS

RESEARCH ARTICLE

Predictability of North Pacific blocking events: Analogue-based analysis of historical MIROC6 simulations

Anupama K. Xavier[1,2] | **Oisín Hamilton**[1,2] | **Davide Faranda**[3,4,5] | **Stéphane Vannitsem**[1]

[1]Dynamical Meteorology and Climatology Unit, Royal Meteorological Institute of Belgium, Brussels, Belgium

[2]Earth and Life Institute, Université catholique de Louvain, Louvain-la-Neuve, Belgium

[3]ESTIMR, Laboratoire des Sciences du Climat et de l'Environnement, Gif-sur-Yvette, Paris, France

[4]London Mathematical Laboratory, London, UK

[5]Laboratoire de Météorologie Dynamique/IPSL, Paris, France

Correspondence
Anupama K. Xavier, Dynamical Meteorology and Climatology Unit, Royal Meterological Institute of Belgium, Uccle, 1180 Brussels, Belgium.
Email: xavier.anupamak@meteo.be

Funding information
European Union's Horizon 2020 research and innovation programme under Marie Skłodowska-Curie, Grant/Award Number: 956396

Abstract

Atmospheric blocking exerts a profound influence on midlatitude circulation, yet its predictability remains elusive, due to intrinsic nonlinearities and sensitivity to initial conditions. While blocking dynamics have been extensively studied, the impact of geographical positioning on predictability remains largely unexplored. This study provides a comparative assessment of the predictability of western and eastern North Pacific blocking events, leveraging analogue-based diagnostics applied to Coupled Model Intercomparison Project Phase 6 (CMIP6) Model for Interdisciplinary Research on Climate, version 6 (MIROC6) simulations. Blocking structures are identified using geopotential height gradient reversal, with their temporal evolution analyzed through trajectory tracking and error growth metrics. Results reveal that eastern blocks exhibit lower predictability, characterized by rapid error divergence and increased mean logarithmic growth rates compared with western blocks. Persistence analysis gives no significant difference between eastern and western North Pacific blocking events. Sensitivity analyses across varying detection thresholds validate the robustness of these findings.

KEYWORDS

analogue-based diagnostics, blocking dynamics, CMIP6 MIROC6 simulations, midlatitude circulation, North Pacific blocking, predictability, trajectory tracking

1 | INTRODUCTION

Atmospheric blocking is a fundamental dynamical phenomenon that influences midlatitude weather evolution by disrupting the typical westerly flow. Characterized by persistent, quasi-stationary high-pressure systems, these blocks can last from several days to weeks, leading to prolonged extreme weather conditions such as heatwaves, cold spells, and heavy precipitation events (Liu, 1994; Masato *et al.*, 2012; Nakamura & Huang, 2018; Rex, 1950; Tibaldi & Molteni, 1990). The North Pacific region is particularly prone to blocking events, which play a key role in modulating weather and climate variability across North America and Eurasia (Park *et al.*, 2024; Woollings *et al.*, 2018).

Despite its recognized impact on regional climate and extreme weather, the predictability of atmospheric blocking remains a challenge in numerical weather

prediction (NWP) and climate modelling. The inherent nonlinear nature of blocking dynamics, along with its sensitivity to initial conditions and complex interactions with large-scale atmospheric waves, contributes to forecast uncertainty (Masato *et al.*, 2012; Matsueda & Palmer, 2018; Pelly & Hoskins, 2003). In the North Pacific, blocking events are typically categorized into two primary regions: western North Pacific (WNP) and eastern North Pacific (ENP) blocks (Davini *et al.*, 2012). Given the substantial downstream effects on weather and climate variability, enhancing understanding of the predictability of these blocking regimes is crucial for improving forecast skill and weather model performance (Breeden *et al.*, 2020; Drouard *et al.*, 2019; Merryfield *et al.*, 2020).

Several studies have examined the predictability of North Pacific blocking using ensemble forecasting methods and model intercomparisons (Leutbecher & Palmer, 2008; Matsueda, 2009; Schiemann *et al.*, 2020). While advancements in global climate models (GCMs) and numerical weather prediction systems have led to some improvements in simulating blocking characteristics, significant biases persist in representing their frequency, persistence (De Luca *et al.*, 2024; Schiemann *et al.*, 2020), and decay (Palmer *et al.*, 2008; Davini and D'Andrea, 2016). The latest generation of Coupled Model Intercomparison Project Phase 6 (CMIP6) models still struggles to capture high-impact extreme events linked to blocking, highlighting a critical gap in understanding the mechanisms governing their predictability (Davini and D'Andrea, 2020).

An overlooked aspect in existing research is the potential influence of the geographical position of a blocking event on its predictability. To date, no systematic studies have been conducted to determine whether the location of blocking relative to major topographical features affects its predictability. Research by Xavier *et al.* (2024), based on a reduced-order atmosphere–land model (Demaeyer *et al.*, 2020), suggests that blocking events positioned to the west of a given topographical feature tend to exhibit lower predictability and greater instability compared with those occurring on the eastern side.

Building on the results of this idealized approach, which suggest boundary constraints can modulate regime stability (Xavier *et al.*, 2024), we ask whether the same predictability differences are evident in a comprehensive model. Using CMIP6 Model for Interdisciplinary Research on Climate, version 6 (MIROC6) daily fields, we analyze North Pacific blocking events with an emphasis on how location relative to basin boundaries (continental margins) influences intrinsic predictability and stability. The spatial structures and geographical distributions reported by (Xavier *et al.*, 2024) closely resemble North Pacific blocks, which, in practice, occur on either the western or eastern side of major basin boundaries; in the physical world, these correspond to the Asian (Russian) and North American (Alaska–west coast) margins of the Pacific. Accordingly, we define two objective boxes that hug these boundaries: an eastern North Pacific box adjacent to Asia (Asian blocks) and a western North Pacific box adjacent to North America (American blocks) (Figure 1). Our hypothesis is that these blocks exhibit a difference in predictability, owing to the geographical position and proximity to the continents, which can be attributed to the differences in background flow and transient eddy activity.

The structure of the article is as follows. Section 2 introduces the data and methodology used for the investigation. In Section 3, properties of the reference–analogue pair are discussed, along with the predictability properties of identified blocking events. The conclusions drawn from the research are provided in Section 4, along with future perspectives for further studies.

2 | DATA AND METHODOLOGY

In this section, we outline the dataset and methodological framework that was used to analyze the predictability of atmospheric blocking in the North Pacific.

2.1 | Data

This study uses the output of the CMIP6 MIROC6 experiment (Tatebe & Watanabe, 2018), in which the atmospheric component has a spatial resolution of approximately $1.4° \times 1.4°$ (T85 spectral resolution, 250 km), covering the period between 1850 and 2014, using the historical scenario. While reanalysis datasets such as the European Centre for Medium-Range Weather Forecasts (ECMWF) Reanalysis Version 5 (ERA5) and the 20th Century Reanalysis have been widely used to study blocking dynamics, we chose not to rely on them here, because this type of analysis has already been addressed extensively in the literature (Compo *et al.*, 2011; Hauser *et al.*, 2024; Thomas *et al.*, 2021). Moreover, MIROC6 provides a substantially longer historical record (1850–2014) than reanalyses, enabling a larger sample size of blocking events for robust statistical evaluation. Importantly, MIROC6 has been shown to exhibit comparatively low bias over the North Pacific compared with ERA5, the 20th Century Reanalysis, and MIROC5 (Lohmann *et al.*, 2024; Tatebe *et al.*, 2019), making it a suitable dataset for our analogue-based predictability analysis. The analysis is based on 500-hPa Z_{500} with a temporal resolution of one day. Although MIROC6 provides multiple ensemble members, only one member (r10i1p1f1) was used here, as the analogue–reference framework (detailed in Section 2.2)

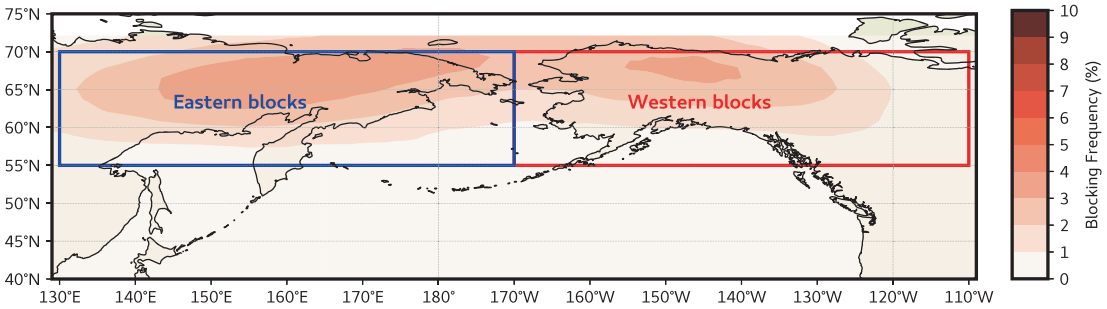

FIGURE 1 Geographical domains used to define the eastern and western North Pacific blocking regions in this study. Both domains span latitudes of 55°N–70°N. The western North Pacific (WNP) block (American) region (red - right box) is bounded between longitudes of 170°W and 110°W (190°E and 250°E), and the eastern North Pacific (ENP) block (Asian) region (blue - left box) between 130°E and 170°W (130°E and 190°E). These regions are highlighted by boxes to facilitate the identification of atmospheric blocking events. The colour gradient represents the blocking frequency over the study region. [Colour figure can be viewed at wileyonlinelibrary.com]

already samples diverse initial conditions in a way analogous to an ensemble. An additional investigation with the other members is worth performing in the future for comparison with the current analysis. For model dependence sensitivity, we repeated the analysis with IPSL-CM6A-LR and MPI-ESM1 historical simulations (daily Z_{500}), processed identically to MIROC6, and results are shown in the supplementary information (Figures S1 and S2).

2.2 | Methodology

The initial step is to identify blocking events in the North Pacific region and classify these into eastern (Asian) or western (American) blocks based on the geographical location. The east and west domains were defined as boxes, which are shown in Figure 1. The colour gradient denotes the blocking frequency calculated using the Davini *et al.* (2012) index (detailed in Section 2.2.1). The blocking frequency is spread out in the eastern region, where as it is lower, and concentrated on the western coast of North America.

2.2.1 | Identifying blocking events

To identify atmospheric blocking events, we employ the meridional gradient reversal method using the 500-hPa Z_{500}, following the approach introduced in Davini *et al.* (2012). This method identifies reversals in the Z_{500} gradient between a northern latitude (denoted GHGN) and a southern latitude (GHGS), and is presented in Equation (1):

$$\mathrm{GHGN}(t,\lambda_0,\Phi_0)=\frac{Z_{500}(t,\lambda_0,\Phi_\mathrm{N})-Z_{500}(t,\lambda_0,\Phi_0)}{\Phi_\mathrm{N}-\Phi_0},$$
$$\mathrm{GHGS}(t,\lambda_0,\Phi_0)=\frac{Z_{500}(t,\lambda_0,\Phi_0)-Z_{500}(t,\lambda_0,\Phi_\mathrm{S})}{\Phi_0-\Phi_\mathrm{S}}, \quad (1)$$

where λ_0 and Φ_0 represent the longitude and latitude of the grid cell, respectively, and t is the given time index. In this study we calculate blocking events at midday UTC on a daily basis, so the variable t is an integer daily index. Φ_0 ranges from 30°N to 75°N. $\Phi_\mathrm{S}=\Phi_0-15°$, $\Phi_\mathrm{N}=\Phi_0+15°$, and $Z_{500}(t,\lambda_0,\Phi)$ denotes the Z_{500} at the specified latitude on day t.

A grid cell is considered to be experiencing instantaneous blocking (IB) if both of the following conditions hold:

$$\mathrm{GHGS}(t,\lambda_0,\Phi_0)>0; \qquad \mathrm{GHGN}(t,\lambda_0,\Phi_0) < -10\ \mathrm{m}(^\circ\mathrm{lat})^{-1}.$$

Davini *et al.* (2012) introduced additional conditions to isolate blocking events that occur over large spatial scales and have temporal persistence. This criterion ensures that only regions that exhibit a strong reversal in the meridional Z_{500} gradient are considered blocking events, filtering out transient anomalies. To do this, large-scale blocks are identified by requiring that the IB condition is satisfied over a longitudinal span of at least 15°.

To include temporal persistence, a blocking event (BE) is detected if a cell that satisfies the large-scale blocking condition occurs within a 5° latitude ×10° longitude box centred on that grid cell for at least five consecutive days.

Secondly, to avoid low-latitude blocks in order to focus on midlatitude blocks and to avoid detecting block-like features from the Tropics, this criterion is included:

$$\mathrm{GHGS}_2(\lambda_0,\Phi_0)=\frac{Z_{500}(\lambda_0,\Phi_\mathrm{S})-Z_{500}(\lambda_0,\Phi_\mathrm{S}-15°)}{15°} \quad (2)$$
$$< -5\ \mathrm{m}(^\circ\mathrm{lat})^{-1}. \quad (3)$$

Hence a blocking event, $BE(t,x,y)$, is defined as follows:

$$BE(t,x,y)=\begin{cases}1 & \text{if criteria from Davini et al (2012) are met,}\\ 0 & \text{otherwise;}\end{cases}$$

TABLE 1 Summary of notations used for blocking detection and frequency measures.

Symbol	Definition
$IB(t,x,y)$	Instantaneous blocking indicator (1 if gradient-reversal condition is satisfied, 0 otherwise)
$BE(t,x,y)$	Blocking event indicator (1 if IB satisfies large-scale and persistence criteria, 0 otherwise)
$AB(x,y)$	Local blocking frequency: fraction of time steps when a grid cell is classified as blocked
$BE\%$	Regional mean blocking frequency: spatial average of $AB(x,y)$ over the study domain

here, t is the time index and x and y are the longitude and latitude of the grid cell.

Once the BE are identified, the time-averaged blocking frequency at each grid cell over the entire analysis period is computed. This metric, denoted as $AB(x,y)$, represents the proportion of time steps that a given grid cell is classified as blocked:

$$AB(x,y) = \frac{\sum_{t\in T} BE(t,x,y)}{\#T},$$

where T is an index of all time steps and $\#T$ represents the number of time steps considered.

To quantify the regional mean blocking frequency $BE_{\%}$, we compute the spatial average of $AB(x,y)$ over the entire study domain, which is given by

$$BE_{\%} = \frac{\sum_{x,y} AB(x,y)}{\#x \cdot \#y}.$$

Here, $\#x$ and $\#y$ denote the total number of grid cells in the longitudinal and latitudinal directions, respectively. This metric provides an estimate of the overall blocking occurrence in the domain.

To retain only significant blocking occurrences, we apply a filtering step: grid cells are classified as part of a blocking region if their local blocking frequency exceeds a fraction α of the regional mean, that is,

$$F(x,y) = \begin{cases} 1, & \text{if } AB(x,y) > \alpha \cdot BE_{\%}, \\ 0, & \text{otherwise.} \end{cases}$$

The filtering coefficient α is a dimensionless sensitivity parameter that allows for the comparison of blocking characteristics across different study areas. It ensures that the detection methodology is not biased by the size of the analysis domain. By applying this filtering criterion, we effectively select blocks that occur over the defined geographical area and have a spatial spread above a given threshold.

A given day t is considered a blocked day if the number of grid cells meeting the blocking condition exceeds a prescribed threshold for the selected α:

$$\sum_{x,y} F(x,y) > N_{\alpha},$$

where N_{α} represents the threshold number of grid cells that must satisfy the blocking condition for the day to be classified as blocked. For further clarification of the definition, please refer to Table 1. The use of an α threshold is necessary, because blocking systems are not distributed uniformly across the predefined ENP and WNP block boxes (Figure 1), but rather occupy portions of them. The distribution of blocking frequency (colour gradient projected on Figure 1) denotes that the blocks identified are not concentrated, but rather spread all over the North Pacific region, with peaks over the ENP and WNP boxes. The standard Davini index flags grid cells that satisfy the gradient-reversal condition, yet, without an additional threshold, small or fragmented detections could be classified as regional blocks. By requiring that at least a fraction α of the domain be blocked, we ensure that only events with a meaningful spatial footprint inside the region are retained. This criterion also normalizes differences between the ENP and WNP domains, making their comparison robust.

Sensitivity tests with α varying between 0 and 1 showed that the number of blocked days changes markedly with threshold choice. For instance, with $\alpha = 0.20$, we identify 532 ENP and 251 WNP blocked days, while with $\alpha = 0.25$ the sample reduces to 337 and 103 days, respectively. Higher thresholds (e.g., $\alpha = 0.30$) lead to an overly restrictive sample (105 ENP, 54 WNP). We therefore selected $\alpha = 0.20$ and $\alpha = 0.25$ as optimal values: they yield event counts consistent with reanalysis-based climatologies (Barriopedro *et al.*, 2006; Carrera *et al.*, 2004; Hwang *et al.*, 2020; Lupo *et al.*, 2019), while preserving the synoptic-scale coherence of the blocking structures. Conducting the analysis with both thresholds allowed us to test the robustness of our conclusions further.

2.2.2 | Tracking blocking events

In the previous section, we described how we identify blocking events $BE(t,x,y)$; however, blocking events are

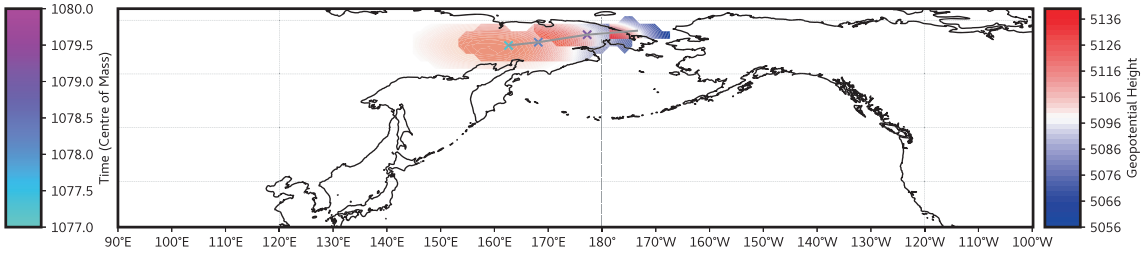

FIGURE 2 Schematic representation of tracking a blocking cluster identified on January 24, 1851 (index 1077). "×" symbols indicate the centre of mass (CoM) of the cluster on each day, coloured by time progression (index), as shown by the left vertical bar. The background colour gradient represents Z_{500}, with values indicated by the right vertical bar. [Colour figure can be viewed at wileyonlinelibrary.com]

defined on a particular day t and provide no information about how they evolve to the next day $t+1$. To allow us to track the same blocking event through time, we use the tracking methodology introduced in Schwierz *et al.* (2004).

For each day in the study period, the grid cells that experience a blocking event ($BE(t,x,y)=1$) are grouped into connected clusters of grid cells. Two blocking events ($BE(t_0,x_1,y_1)=1$ and $BE(t_0,x_2,y_2)=1$) are defined as connected if a path exists between the two events that passes through grid cells (x_i,y_i), where, for all transiting grid cells, $BE(t_0,x_i,y_i)=1$, and each grid cell shares an edge. In other words, two blocking events are in the same blocking cluster if they are connected to one another with other non-zero blocking events. These clusters were identified using the python library SciPy (Virtanen *et al.*, 2020), which identifies connected regions in pixelated images (Steinfeld, 2020).

A blocking cluster at day $t+1$ is considered as the evolution of the cluster at day t if they overlap sufficiently in space. This overlap is calculated by taking the spatial intersection of the clusters from one day to the next. The threshold is calculated by comparing the number of grid cells in the intersection with the number of grid cells in the cluster on the first day t. If the intersection covers at least half of the original cluster, we consider the cluster at $t+1$ to be the evolution of the cluster from time t. More concretely, let $C_i(t)$ be a cluster of blocking events at time t, and $C_j(t+1)$ another cluster on the next day. If $|C_i(t)\cap C_j(t+1)|/|C_i(t)|>0.5$, then we assume $C_i(t)$ evolves into $C_j(t+1)$. Here, we use $|\cdot|$ to denote the number of grid cells in each cluster. In this study, we only track blocking clusters that have a single predecessor and a single successor cluster, thus removing any blocking clusters that split or merge from other blocks. An example of the process of tracking a particular blocking cluster is shown in Figure 2.

Lastly, we calculate the centre of mass of each cluster, which provides a representative location for each block, enabling the identification of displacement and persistence while minimizing the influence of irregular block shapes and fragmented patterns. The centre of mass is weighted using Z_{500}. We apply this weighting as the centre of the blocking cluster, as in this study we are using Z_{500} as the measure for identifying blocking events.

2.2.3 | Finding analogues

Once blocked days are identified, we determine one analogue for each blocked day based on a similarity criterion. The analogue search is performed using a distance metric to compare atmospheric states.

The fundamental concept of assessing atmospheric predictability through analogue-based error diagnostics has been discussed widely in the meteorological literature (Lorenz, 1969). We build upon these foundational ideas to evaluate and compare the predictability of ENP and WNP blocking events. A key metric in those early analyses was the reference–analogue error, often quantified with a (possibly weighted) root-mean-square height difference to measure deviations between two atmospheric states. Reference–analogue errors arise from inherent dynamical differences between effectively occurring atmospheric situations, in particular for blocking events that share similar large-scale structures but evolve differently in time (Faranda *et al.*, 2017, 2023; Yiou *et al.*, 2007). The progression of analogue errors has been used as a diagnostic of blocking stability, helping to distinguish persistent from transient regimes (Plaut & Vautard, 1994), and, more broadly, as a data-driven alternative to ensemble approaches for studying flow recurrence (Yiou, 2014).

Following Lorenz (1969), an analogue is assumed to reproduce the spatial distribution of the reference state plus a small deviation. By selecting, for each blocked day, the analogue that minimizes the distance to its reference, the initial deviation is reduced, and comparing their subsequent evolution provides a local (in phase space) estimate of predictability for that reference block.

For the reference block, on day t_r, its corresponding analogue day t_a is selected from the dataset based on a

minimum distance criterion. The similarity between two atmospheric states is assessed using the spatial distribution of Z_{500}. Here, X_t denotes the atmospheric state vector at time t, represented by the gridded Z_{500} over the selected spatial domain. It characterizes the synoptic-scale circulation pattern for a given day. The Euclidean distance is used to quantify the difference between the reference blocked day's Z_{500} field and that of any candidate day, as follows:

$$d(X_{t_r}, X_t) = \|Z_{500}(t_r) - Z_{500}(t)\|, \tag{4}$$

where $d(X_{t_r}, X_t)$ represents the Euclidean distance between the Z_{500} fields at times t_r and t. The dataset consists of the spatial distribution of Z_{500}, and the goal is to identify an analogue block on day t_a such that

$$t_a = \underset{|t-t_r|\geq\Delta t_{min}}{\operatorname{argmin}} \; d(X_{t_r}, X_t), \tag{5}$$

where $\Delta t_{min} = 5$, as in Davini *et al.* (2012), which ensures a minimum temporal separation of at least 5 days between the blocked day and its analogue (Diao *et al.*, 2006). This constraint prevents the selection of analogues that are too close in time to the original reference block, thereby avoiding redundancy due to short-term atmospheric persistence.

The analogue search procedure involves iterating over all available time steps, computing the Euclidean distance between the Z_{500} distributions, and selecting the time step t_a that satisfies both the minimum distance criterion and the temporal separation condition. This approach ensures that each blocked day is assigned an analogue day that exhibits the most similar large-scale Z_{500} distribution, providing insights into the recurrence of similar atmospheric circulation patterns.

The traditional analogue method for assessing error evolution (Lorenz, 1969) is not suitable in this context, as it fails to account for differences in predictability between eastern and western blocking regions due to the displacement of blocking events following their initial identification. Therefore, error evolution based on the centre of mass is employed in the current study to capture the spatial progression of blocking features better.

After identifying the reference and analogue blocking pairs, we track their temporal evolution using the block-tracking algorithm, as explained in Section 2.2.2. The trajectories of the reference and analogue blocks are denoted by $\mathbf{X}_r(t)$ and $\mathbf{X}_a(t)$, respectively, representing the latitude and longitude coordinates of the blocking centre over time. Unlike traditional analogue approaches that select several analogues per reference state (often with relatively large initial errors), we select only the single closest analogue for each blocked day. This reduces the initial mismatch and ensures that subsequent divergence reflects the intrinsic instability of the block rather than poor analogue choice. By applying this systematically to all blocked days identified, the methodology mimics an ensemble evaluation across hundreds of cases, providing a probabilistic measure of predictability for ENP and WNP blocks.

2.2.4 | Measure of predictability

To assess the predictability of ENP and WNP blocking events, we analyze the error evolution between the trajectories of the reference and analogue blocking pairs. The tracking of these blocking days is performed using a block-tracking algorithm (Section 2.2.2) that follows the movement of the centre of mass of each identified blocking system over time.

The error evolution between the reference and analogue blocking trajectories is computed using the Haversine distance, which measures the great-circle distance between two points on the Earth's surface:

$$d_H(\lambda_r, \phi_r, \lambda_a, \phi_a) = 2R \arcsin \times \left(\sqrt{\sin^2\left(\frac{\phi_a - \phi_r}{2}\right) + \cos(\phi_r)\cos(\phi_a)\sin^2\left(\frac{\lambda_a - \lambda_r}{2}\right)} \right), \tag{6}$$

where d_H is the Haversine distance, $R = 6371$ km is the Earth's radius, and (λ, ϕ) represent the longitude and latitude of the reference (λ_r, ϕ_r) and analogue (λ_a, ϕ_a) blocking centres.

For each pair of reference and analogue trajectories, we compute the error evolution at time t as

$$E_i(t) = d_H\left(\mathbf{X}_{r,i}(t), \mathbf{X}_{a,i}(t)\right), \tag{7}$$

where $E_i(t)$ represents the displacement error for the ith reference–analogue pair at time step t. The errors are recorded for all analogue pairs and stored in an error matrix, allowing for further statistical analysis.

For each region and threshold α, we rank all reference–analogue pairs by their initial Euclidean distance at t_0 and analyze the first 50 as the baseline set and the first 75 as a sensitivity set, a choice that controls the initial error, so that subsequent divergence reflects dynamics rather than analogue mismatch, and preserves equal sample sizes across ENP/WNP for robust bootstrap inference; we avoid a fixed-percentage selection because the total number of blocks identified varies markedly across regions and α, which would otherwise yield unequal sample sizes and heterogeneous uncertainty. This enhances

the robustness of the error growth analysis by minimizing the influence of initial-condition differences and allowing for a meaningful assessment of dynamical divergence over time.

The statistical distribution of errors is analyzed by computing the mean and standard deviation of the error evolution across all reference–analogue pairs. To estimate the uncertainty in the error evolution, a bootstrap resampling technique is applied and the 95% confidence interval (CI) is obtained.

To assess the exponential growth of initial uncertainties, we compute the logarithmic growth rate for each pair at lead time τ and increment $\Delta\tau$, which quantifies the sensitivity of blocking events to small initial perturbations:

$$\lambda_i(\tau) = \frac{1}{\Delta\tau} \ln\left(\frac{E_i(\tau + \Delta\tau)}{E_i(\tau)}\right), \tag{8}$$

where $E_i(\tau)$ is the displacement error for the ith pair at lead time τ and $\Delta\tau$ is the time increment.

The mean logarithmic growth rate at each lead time is then computed by averaging over all analogue pairs:

$$\overline{\lambda}(\tau) = \frac{1}{N}\sum_{i=1}^{N} \lambda_i(\tau), \tag{9}$$

where N is the total number of analogue realizations. Comparing $\overline{\lambda}$ for ENP and WNP North Pacific blocks reveals differences in their intrinsic predictability characteristics.

2.2.5 | Persistence of blocking events

To quantify persistence, we define the lifetime of a blocking event based on its tracked trajectory over time. Given a blocking system that is identified at time t_0 and remains detectable until time t_f, its persistence P is given by $P = t_f - t_0 + 1$, where t_0 is the initial and t_f the final time step where the block is detected.

This methodology enables the analysis of the persistence of blocking events, providing ideas about their stability and potential for long-term atmospheric impacts. Overall, the analysis above provides both a deterministic and a probabilistic measure of stability through the persistence and mean logarithmic growth-rate computation, allowing for a comprehensive assessment of the stability and comparability of North Pacific blocking events. To ensure statistical robustness of the analogue-based predictability diagnostics, we analyze all months (annual sampling). Given the strict spatial and persistence criteria in the blocking definition, seasonal stratification (e.g., December–January–February (DJF) versus June–July–August (JJA)) would reduce the number of ENP (Asian) or WNP (American) blocking events substantially and inflate the sampling uncertainty of growth-rate estimates and their confidence intervals.

3 | RESULTS AND DISCUSSION

3.1 | Composite of geopotential height (Z_{500}) on ENP (Asian) and WNP (American) blocking days

Figure 3 shows the composite (temporal mean) 500-hPa Z_{500} field on days classified as blocked, computed using the methodology detailed in Section 2.2 when $\alpha = 0.25$. The classification effectively distinguishes between the ENP (Asian) and WNP (American) blocking patterns. The spatial distribution of Z_{500} reveals that ENP blocks are concentrated primarily over the Aleutian region of Russia. This indicates that most identified ENP blocks exhibit blocking highs in this region. Conversely, WNP blocks exhibit a more extensive distribution, with blocking highs dispersed across Alaska. The WNP blocks are characterized by an intense high-pressure system, as evident from the deeper red-shaded regions, compared with the ENP blocks. While the ENP block presents a confined structure, the WNP block's influence extends over a broader region of North America. This spatial distinction suggests potential differences in the dynamical characteristics and downstream impacts of these blocking patterns.

Results for $\alpha = 0.20$ (Appendix A, Figure A1) show similar spatial patterns, but with a larger number of blocking days identified, consistent with the more relaxed threshold. These are included as sensitivity tests to demonstrate robustness.

3.2 | Persistence of ENP (Asian) and WNP (American) blocks

In this section, persistence of the ENP and WNP blocks was calculated for $\alpha = 0.20$ and $\alpha = 0.25$.

Figure 4 presents the probability density distribution of blocking persistence, with a fitted gamma distribution applied to the entire dataset. The initial portion of the distribution exhibits a strong overlap between ENP and WNP blocks, particularly for block lifetimes up to 10 days. Beyond this threshold, the tails of the distributions diverge significantly, indicating a higher occurrence of long-lived ENP blocks compared with WNP blocks. ENP blocks demonstrate a tendency to persist beyond 10 days, whereas WNP blocks exhibit a sharper decline in frequency for extended durations.

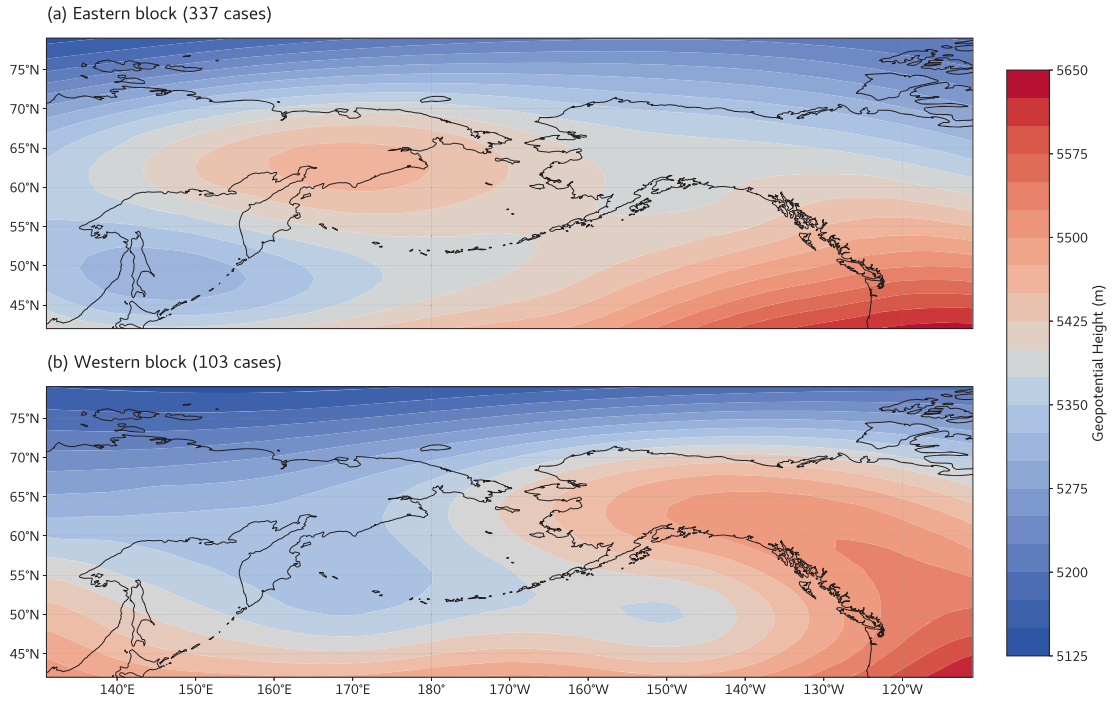

FIGURE 3 Composite (temporal mean) of Z_{500} (m) conditioned on blocked days for (a) ENP blocks and (b) WNP blocks, obtained using the methodology described in Section 2 with $\alpha = 0.25$. The composite is computed over the base period from 1850–2014. 337 ENP blocks and 103 WNP blocks is identified with this threshold. [Colour figure can be viewed at wileyonlinelibrary.com]

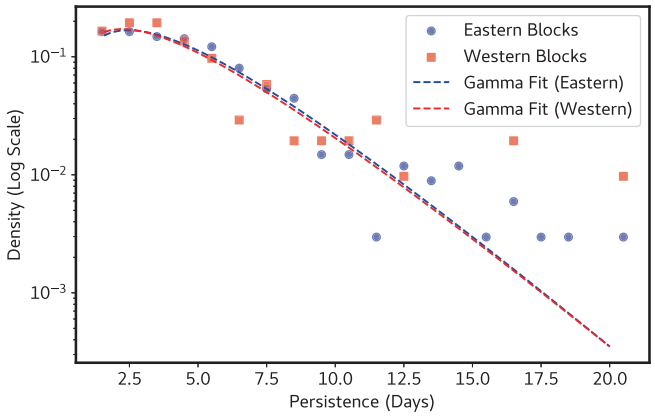

FIGURE 4 Log-scaled density distribution of blocking persistence (in days) for ENP and WNP blocks with $\alpha = 0.25$. The fitted gamma distributions for both cases are also shown. [Colour figure can be viewed at wileyonlinelibrary.com]

When the sample size is increased by reducing the selection threshold to $\alpha = 0.20$ (Figure A2), the initial portion of the distribution remains substantially unchanged. However, the disparity in long-lived blocking events diminishes, with ENP and WNP blocks displaying a more balanced distribution of extended persistence.

The observed changes with decreasing α can be attributed to the inclusion of a broader range of blocking events, incorporating shorter-lived and less persistent blocks that were previously excluded under a stricter selection criterion. Given the constraints of our methodology, we did not identify notable differences in persistence between ENP (Asian) and WNP (American) blocking events.

3.3 | Structural comparison of reference and analogue blocks

This section presents a representative case illustrating the Z_{500} fields for a typical ENP and WNP block and their nearest-neighbour analogues. In Figure 5, the spatial distribution of Z_{500} of a selected ENP and WNP block and its corresponding analogues are depicted. In order to identify the difference in the distributions, the anomaly between them is also computed.

Figure 5a,c represents the typical analogue pair for the ENP block, while Figure 5b,d corresponds to the WNP block pair. Both reference–analogue pairs exhibit a high degree of similarity in their Z_{500} distributions, indicating that the analogue blocks capture the large-scale structure of the reference blocks effectively. The differences between the selected reference and analogue blocks, depicted in Figure 5e,f, reveal anomalies within a range of ±720 m, which is significantly smaller than the typical anomaly range of ±1000 m observed between two

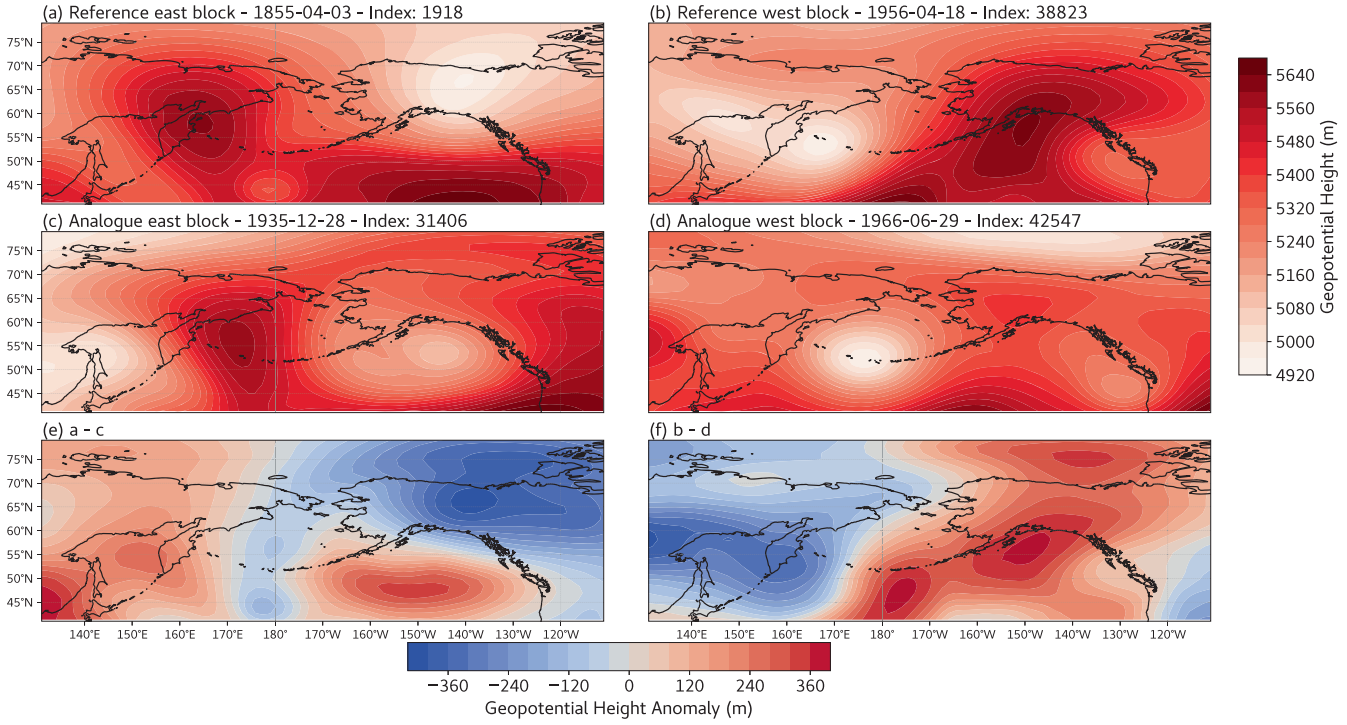

FIGURE 5 Z_{500} distribution of the reference (a) ENP and (b) WNP blocks, respectively, and (c,d) their analogue blocks. Panels (e) and (f) depict the Z_{500} anomalies between the typical and analogue blocks for the ENP and WNP cases, respectively. This example is drawn randomly from the $\alpha = 0.25$ first-50 subset. [Colour figure can be viewed at wileyonlinelibrary.com]

randomly selected blocking days. This suggests that the analogue blocks resemble their respective reference blocks much more closely, with only minor variations in intensity and spatial extent. The anomaly patterns highlight localized differences, which may be attributed to transient synoptic-scale features or differences in block persistence. These findings reinforce the reliability of the analogue approach in identifying predictability and stability of atmospheric blocking patterns.

3.4 | Stability and predictability of identified blocks

Figure 6a illustrates the evolution of the average error for the first 50 reference–analogue pairs, quantifying the divergence between their trajectories. The shaded regions denote the standard deviation, capturing the variability in error growth across different blocking cases. The results indicate that the trajectories of ENP blocks diverge more rapidly than those of WNP blocks, suggesting that ENP blocks exhibit lower stability.

Figure 6b presents the bootstrap mean error for both ENP and WNP blocks, along with their respective 95% CIs. The use of the bootstrap method (with replacement) enhances statistical robustness by resampling the data to estimate uncertainty. The widening confidence intervals over time reflect an increasing separation between reference and analogue blocks, reinforcing the idea that blocking predictability diminishes with lead time. This decline is pronounced for ENP blocks, indicating a greater rate of divergence compared with WNP blocks. Curves end when too few pairs remain because one or both blocks terminate or splits, so the valid sample becomes small. The bootstrap shading shows the 95% CI of the mean, naturally narrower (scaling as $\propto 1/\sqrt{n}$) than the $\pm 1\ \sigma$ shading in Figure 6a, which reflects the spread across individual cases, and it terminates earlier because we require a minimum effective sample size for stable intervals; by contrast, the $\pm 1\ \sigma$ shading can be shown for smaller samples and therefore may extend further in lead.

Figure 6c depicts the averaged growth rate of the logarithm of the error, which is equivalent to the definition of the Lyapunov exponents, which characterizes how quickly small perturbations in initial conditions amplify, offering insight into the chaotic behaviour of atmospheric blocking. Higher values correspond to increased instability and reduced predictability. Note that, in the case of a pure exponential behaviour along the dominant local instability, this averaged growth rate would have been constant as a function of time.

The results suggest that ENP blocks exhibit larger logarithmic growth rate, implying a larger sensitivity to initial perturbations and, consequently, lower predictability

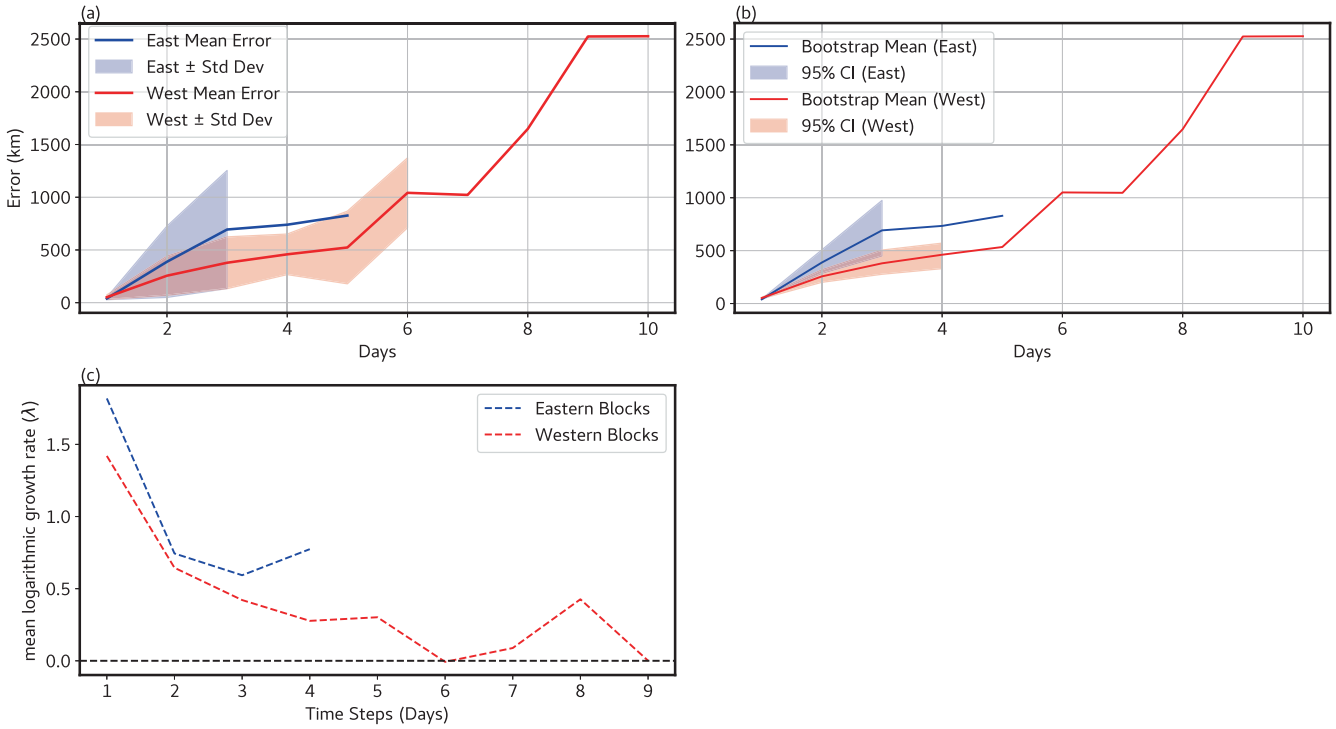

FIGURE 6 Evolution of error and logarithmic growth rate for ENP and WNP blocks, considering $\alpha = 0.25$ and the first 50 reference–analogue pairs with the smallest initial error. (a) Mean error growth over time for ENP and WNP blocks, with shaded regions representing the standard deviation. (b) Bootstrap mean error with 95% confidence intervals for both block types. Curves terminate where too few pairs remain because one or both blocks cease or splits.(c) Mean logarithmic growth rate over time, comparing the stability characteristics of ENP and WNP blocks. [Colour figure can be viewed at wileyonlinelibrary.com]

compared with WNP blocks. Over time, the growth rate decreases for both cases, which could indicate either the progressive saturation of the error, as expected when the error becomes large (Nicolis *et al.*, 1995; Vannitsem & Nicolis, 1997), or the increase of predictability of the blocking after its onset. Disentangling one from the other would require us to make model experiments with very small initial-condition errors at different stages of the development of blocking. The analysis above, however, indicates the strong instability of ENP blocks over WNP blocks.

A key clarification is warranted regarding the nature of positional error growth in the blocking events shown. As discussed in details in Bohr *et al.* (1998), one should distinguish between Eulerian and Lagrangian Lyapunov instabilities. The former are associated with the difference in the initial state of the background flow, while the latter are related to the spatial difference between the positions of the structures of interest, that is, the blocking events. Here, both Lagrangian and Eulerian errors are affecting the dynamics, and one cannot distinguish between the two here, as they are intertwined. In Bohr *et al.* (1998), it is also shown that, in the presence of both errors, the largest exponent among the Lagrangian and Eulerian Lyapunov instabilities is controlling the error evolution. We thus suspect that, in our case, the maximum Lyapunov exponent between the Eulerian and Lagrangian approaches is at play. The first value of Figure 6c can then be viewed as an estimate of the dominant local (in physical space) Lyapunov instability of the blocking events.

The same analysis was repeated for the first 75 reference–analogue pairs, as shown in Figure 7. In Figure 7a,b, the average error evolution for ENP and WNP blocks appears nearly indistinguishable, indicating reduced contrast compared with Figure 6a,b. However, a slight difference remains, with ENP blocks still exhibiting a marginally higher rate of error growth than their WNP counterparts. The variability, quantified as the spread in error evolution across the reference–analogue pairs calculated using both the standard deviation and the bootstrap 95% confidence interval, overlaps for both cases. This reduction in the difference in average error evolution suggests that increasing the sample size introduces greater diversity in blocking characteristics with larger initial-condition errors, leading to a broader representation of stability and transition behaviours. As a result, the contrast between ENP and WNP blocks initially observed diminishes, highlighting the influence of sample selection on assessing blocking predictability. The mean logarithmic growth rate in Figure 7 shows a comparable difference

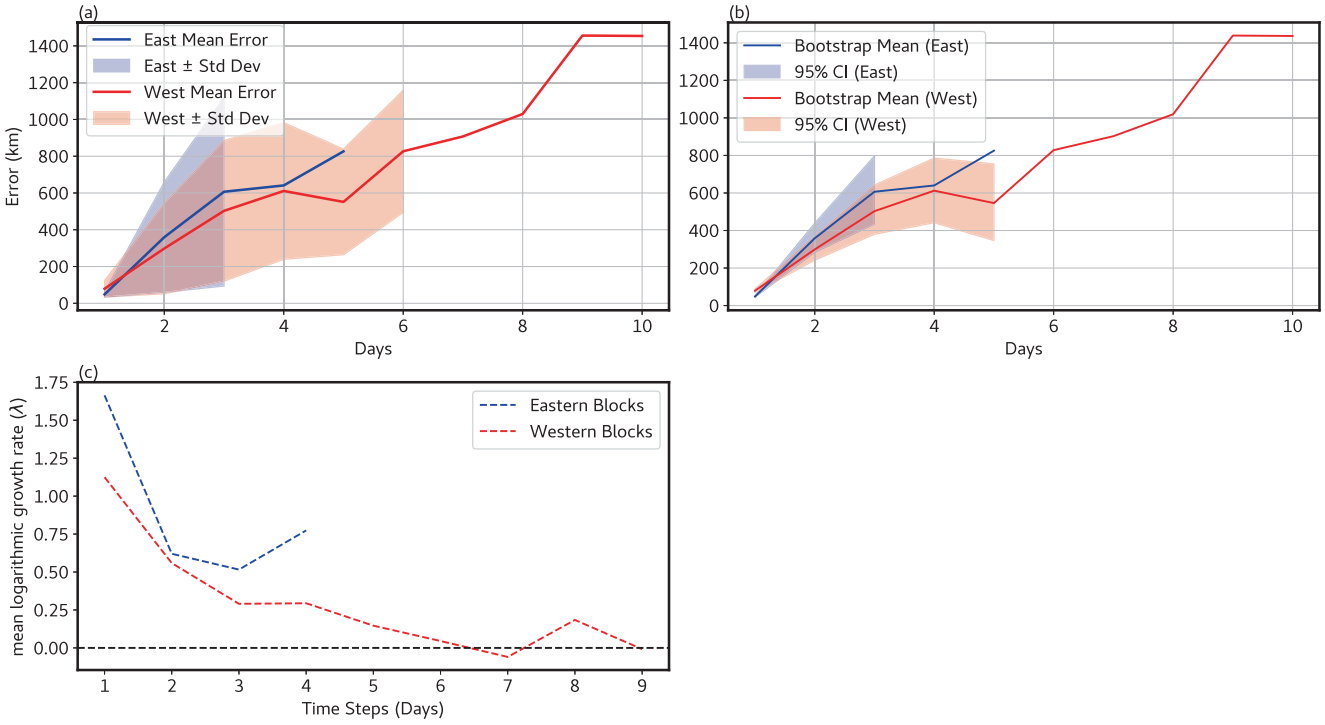

FIGURE 7 Same as Figure 6, but with $\alpha = 0.25$, considering the first 75 reference–analogue pairs. [Colour figure can be viewed at wileyonlinelibrary.com]

for both cases by highlighting lower predictability for ENP blocks, as in Figure 6. Despite increasing the sample size from 50 to 75 cases, the logarithmic growth rate continues to exhibit significantly different values for ENP and WNP blocks. This suggests that the inherent instability of ENP blocks is a fundamental characteristic, less dependent on the number of selected cases.

The analysis was repeated for $\alpha = 0.20$ (the figures are included in Appendix A) and the resulting error evolution and mean logarithmic growth rate for the first 50 cases are presented in Figure A3. The mean error evolution exhibits a similar pattern to previous analyses, with higher values for ENP blocks, reaffirming their lower stability. However, the logarithmic error growth rate (Figure A3c) shows a distinct behaviour: initial differences between ENP and WNP blocks gradually diminish, leading to an overlap on day 2. As time progresses, the divergence becomes significant again, particularly on days 3, 4, and 5, supporting further the conclusion that ENP blocks are inherently more unstable than WNP blocks.

For the first 75 cases (Figure A4), a similar pattern emerges. Initially, ENP blocks exhibit higher error values, but beyond the fifth day the error evolution of ENP and WNP blocks becomes more comparable, leading to an overlap. The logarithmic error growth rate follows a non-monotonic behaviour: higher initial values for ENP blocks, followed by relatively lower values on days 3 and 4, and a subsequent increase on day 5.

Reducing the threshold α from 0.25 to 0.20 increases sensitivity to smaller-scale variability by allowing a broader range of blocking events. This broader inclusion introduces greater variability in error growth patterns, as reflected in the non-monotonic behaviour of logarithmic error on days 3 and 4. With a less stringent analogue selection, initial differences between reference and analogue blocks are slightly larger, which may explain overlapping growth phases—such as day 2 for the 50-case scenario and day 5 for the 75-case scenario—before divergence occurs. These effects are amplified further in larger samples, where a mix of more persistent and less stable blocks leads to alternating phases of stronger and weaker error growth.

In contrast, using a stricter threshold of $\alpha = 0.25$ ensures the selection of only the most structurally similar blocking events, making the differences in their instability characteristics more apparent. Despite the added variability introduced at $\alpha = 0.20$, the underlying instability of ENP blocks remains evident, as they consistently exhibit higher error values and larger mean logarithmic growth rates over time.

4 | CONCLUSION

This study investigates the predictability of eastern and western North Pacific atmospheric blocking events using

an analogue-based approach. Our results provide a dynamical complement to established descriptions of North Pacific blocking occurrence and structure. Prior studies have documented robust blocked day climatologies and regional preferences based on gradient-reversal indices and related diagnostics (e.g., Barriopedro *et al.*, 2006; Davini *et al.*, 2012; Lupo *et al.*, 2019), including over the Kuroshio–Oyashio Extension and Gulf of Alaska sectors. The composite Z_{500} fields conditioned on blocked days (Figure 3) align with these preferred locations, while our analogue-based metrics quantify how quickly initially similar states diverge, thereby translating structural preferences into a finite-time predictability perspective.

The east–west asymmetry we find, systematically faster divergence (larger mean logarithmic growth rates) for ENP blocks, fits with well-known contrasts in the background flow. In the northwest Pacific near the Russian coast and the Kuroshio–Oyashio Extension (ENP block region), the jet entrance region, sharp sea-surface temperature fronts, and strong baroclinicity favour frequent wave-packet genesis, active transient eddy forcing, and Rossby-wave breaking, all of which enhance sensitivity to small perturbations and shorten intrinsic predictability (Hwang *et al.*, 2020; Che *et al.*, 2021; Masato *et al.*, 2012; O'Reilly & Czaja, 2015; Qiu *et al.*, 2017; Woollings *et al.*, 2018). By contrast, many WNP blocks occur downstream of the jet core, where ridges can be more quasi-stationary and sometimes anchored by coastal or orographic influences, yielding slower error growth and longer predictability horizons (Breeden *et al.*, 2020; Neal *et al.*, 2022; Woollings *et al.*, 2018). In this view, background wave dispersion and transient eddy forcing modulate blocking stability in a way that naturally produces lower predictability for ENP than for WNP, even when initial structures are similar (Hwang *et al.*, 2020; Woollings *et al.*, 2018).

Methodologically, our analogue framework complements persistence-based descriptors and ensemble-forecast evaluations of blocking predictability (Matsueda, 2009; Plaut & Vautard, 1994). Persistence distributions quantify how long blocks last but do not capture sensitivity to small perturbations directly. Ensemble forecasts provide such sensitivity, but can be model- and configuration-dependent. By contrast, the analogue growth-rate diagnostic we employ computed from reference–analogue pairs in Z_{500} and summarized across many cases offers a model-agnostic, data-driven estimate of local (phase-space) predictability, in the spirit of classical analogue ideas (Lorenz, 1969; Yiou, 2014) and more recent dynamical-system applications to midlatitude regimes (Faranda *et al.*, 2017, 2023; Yiou *et al.*, 2007).

These findings also speak about model evaluation. MIROC6 exhibits relatively small biases over the North Pacific blocking sector compared with commonly used reanalyses (Lohmann *et al.*, 2024), and our east–west contrast persists across reasonable thresholds ($\alpha = 0.20, 0.25$) and sample choices (first 50 or first 75). This indicates that analogue-based growth rates provide a compact benchmark for assessing whether climate models reproduce not only the occurrence of blocks but also their intrinsic predictability, complementing standard blocked-day counts and persistence metrics. As a model-dependence sensitivity test, we repeated the full pipeline with IPSL-CM6A-LR and MPI-ESM1 ($\alpha = 0.25$; first 50 nearest pairs; see Figures S1 and S2 in the supplementary material): MIROC6 retains a clear ENP > WNP early-time divergence, whereas IPSL-CM6A-LR shows only a weak ENP–WNP contrast, and in MPI-ESM1 the reference–analogue pair's initial separation for the ENP block is substantially larger (≈ 693 km), which raises mean error levels, yet the mean logarithmic growth rate that evaluates finite-time divergence relative to the initial mismatch still yields lower predictability for ENP, consistent with MIROC6. This model dependence aligns with independent assessments of North Pacific blocking biases (Lohmann *et al.*, 2024), suggesting that analogue-based predictability diagnostics are most informative when applied to models with realistic blocking occurrence and structure.

Our results show that blocks adjacent to the Asian boundary (ENP) exhibit systematically faster early-time divergence than blocks adjacent to the North American boundary (WNP), implying shorter intrinsic predictability for ENP. This east–west contrast persists across thresholds and sample sizes and is consistent with the view that basin-scale boundary constraints modulate regime stability, extending the idealized finding of Xavier *et al.* (2024) to a comprehensive GCM.

Looking forward, several extensions could deepen and broaden the analysis. First, a seasonal decomposition (e.g., DJF versus JJA) will be pursued when event counts permit, complementing the annual sampling adopted here for robust uncertainty quantification. Beyond Z_{500} fields and centre-of-mass tracking, we will incorporate dynamical diagnostics, such as potential vorticity gradients, wave activity fluxes, and Rossby-wave breaking metrics to attribute the east–west contrast to specific mechanisms. We will also analyze additional MIROC6 ensemble members to contrast inter-member behaviour and, where appropriate, pool events to increase statistical power. In parallel, we will benchmark the methodology against reanalysis datasets, provided enough blocking events can be gathered. Finally, we will assess metric dependence by varying blocking indices and thresholds and applying modest spatial smoothing. Together, these steps aim to refine mechanistic

attribution and test the generality of the east–west predictability asymmetry.

ACKNOWLEDGEMENTS

We thank Francesco Ragone and Mireia Ginesta for helpful discussions and Jonathan Demaeyer for technical support. Anupama K. Xavier has received funding from the European Union's Horizon 2020 research and innovation programme under the Marie Sklodowska–Curie grant agreement no. 956396. O. Hamilton has received funding from the European Union's Horizon 2020 research and innovation programme under the Marie Sklodowska–Curie grant agreement no. 956170, as well as through the "Fédération Wallonie–Bruxelles" with the instrument "Fonds Spéciaux de Recherche". We appreciate the rigorous and constructive reviews provided by two anonymous referees, Dr Paolo De Luca, and the editor Dr Sebastian Schemm, which enhanced the quality of this article.

CONFLICTS OF INTEREST

The authors declare no conflicts of interest.

DATA AVAILABILITY STATEMENT

We used CMIP6 MIROC6 historical (Tatebe & Watanabe, 2018) simulations for the study, which can be downloaded from the ESGF metagrid website at https://aims2.llnl.gov/. Code used for the study can be produced upon request.

ORCID

Anupama K. Xavier https://orcid.org/0000-0002-9783-8322
Oisín Hamilton https://orcid.org/0000-0002-0447-1657
Davide Faranda https://orcid.org/0000-0001-5001-5698
Stéphane Vannitsem https://orcid.org/0000-0002-1734-1042

REFERENCES

Barriopedro, D., García-Herrera, R., Lupo, A.R. & Hernández, E. (2006) A climatology of Northern Hemisphere blocking. *Journal of Climate*, 19(6), 1042–1063.

Bohr, T., Jensen, M.H., Paladin, G. & Vulpiani, A. (1998) *Dynamical systems approach to turbulence*. Cambridge: Cambridge University Press (Cambridge Nonlinear Science Series).

Breeden, M.L., Hoover, B.T., Newman, M. & Vimont, D.J. (2020) Optimal North Pacific blocking precursors and their deterministic subseasonal evolution during boreal winter. *Monthly Weather Review*, 148(2), 739–761.

Carrera, M., Higgins, R. & Kousky, V. (2004) Downstream weather impacts associated with atmospheric blocking over the northeast Pacific. *Journal of Climate*, 17(24), 4823–4839.

Che, Z., Yao, Y. & Zhong, L. (2021) Wintertime sea surface temperature front around the Kuroshio Extension and its impact on North Pacific blocking. *International Journal of Climatology*, 41(3), 1905–1926.

Compo, G.P., Whitaker, J.S., Sardeshmukh, P.D., Matsui, N., Allan, R.J., Yin, X. et al. (2011) The Twentieth Century Reanalysis Project. *Quarterly Journal of the Royal Meteorological Society*, 137, 1–28.

Davini, P. & D'Andrea, F. (2016) Northern Hemisphere atmospheric blocking representation in global climate models: twenty years of improvements? *Journal of Climate*, 29(24), 8823–8840.

Davini, P. & D'Andrea, F. (2020) From CMIP3 to CMIP6: Northern Hemisphere atmospheric blocking simulation in present and future climate. *Journal of Climate*, 33(23), 10021–10038.

Davini, P., Cagnazzo, C., Gualdi, S. & Navarra, A. (2012) Bidimensional diagnostics, variability, and trends of Northern Hemisphere blocking. *Journal of Climate*, 25(19), 6496–6509.

De Luca, P., Jiménez-Esteve, B., Degenhardt, L., Schemm, S. & Pfahl, S. (2024) Enhanced blocking frequencies in very-high resolution idealized climate model simulations. *Geophysical Research Letters*, 51(22), e2024GL111016.

Demaeyer, J., De Cruz, L. & Vannitsem, S. (2020) QGS: a flexible Python framework of reduced-order multiscale climate models. *Journal of Open Source Software*, 5(56), 2597.

Diao, Y., Li, J. & Luo, D. (2006) A new blocking index and its application: blocking action in the Northern Hemisphere. *Journal of Climate*, 19(19), 4819–4839.

Drouard, M., Kornhuber, K. & Woollings, T. (2019) Disentangling dynamic contributions to summer 2018 anomalous weather over Europe. *Geophysical Research Letters*, 46(21), 12537–12546.

Faranda, D., Messori, G. & Yiou, P. (2017) Dynamical proxies of North Atlantic predictability and extremes. *Scientific Reports*, 7(1), 41278.

Faranda, D., Messori, G., Jezequel, A., Vrac, M. & Yiou, P. (2023) Atmospheric circulation compounds anthropogenic warming and impacts of climate extremes in Europe. *Proceedings of the National Academy of Sciences*, 120(13), e2214525120.

Hauser, S., Teubler, F., Riemer, M., Knippertz, P. & Grams, C.M. (2024) Life cycle dynamics of Greenland blocking from a potential vorticity perspective. *Weather and Climate Dynamics*, 5, 633–658.

Hwang, J., Martineau, P., Son, S.W., Miyasaka, T. & Nakamura, H. (2020) The role of transient eddies in North Pacific blocking formation and its seasonality. *Journal of the Atmospheric Sciences*, 77(7), 2453–2470.

Leutbecher, M. & Palmer, T.N. (2008) Ensemble forecasting. *Journal of Computational Physics*, 227(7), 3515–3539.

Liu, Q. (1994) On the definition and persistence of blocking. *Tellus. Series A, Dynamic Meteorology and Oceanography*, 46(3), 286–298.

Lohmann, R., Purr, C. & Ahrens, B. (2024) Northern Hemisphere atmospheric blocking in CMIP6 climate projections using a hybrid index. *Journal of Climate*, 37(24), 6605–6625.

Lorenz, E.N. (1969) Atmospheric predictability as revealed by naturally occurring analogues. *Journal of Atmospheric Sciences*, 26(4), 636–646.

Lupo, A.R., Jensen, A.D., Mokhov, I.I., Timazhev, A.V., Eichler, T. & Efe, B. (2019) Changes in global blocking character in recent decades. *Atmosphere*, 10(2), 92.

Masato, G., Hoskins, B. & Woollings, T.J. (2012) Wave-breaking characteristics of midlatitude blocking. *Quarterly Journal of the Royal Meteorological Society*, 138(666), 1285–1296.

Matsueda, M. (2009) Blocking predictability in operational medium-range ensemble forecasts. *Sola*, 5, 113–116.

Matsueda, M. & Palmer, T. (2018) Estimates of flow-dependent predictability of wintertime Euro-Atlantic weather regimes in medium-range forecasts. *Quarterly Journal of the Royal Meteorological Society*, 144(713), 1012–1027.

Merryfield, W.J., Baehr, J., Batté, L., Becker, E.J., Butler, A.H., Coelho, C.A. et al. (2020) Current and Emerging Developments in Subseasonal to Decadal Prediction. *Bulletin of the American Meteorological Society*, 101(6), E869–E896.

Nakamura, N. & Huang, C.S. (2018) Atmospheric blocking as a traffic jam in the jet stream. *Science*, 361(6397), 42–47.

Neal, E., Huang, C.S. & Nakamura, N. (2022) The 2021 Pacific Northwest heat wave and associated blocking: meteorology and the role of an upstream cyclone as a diabatic source of wave activity. *Geophysical Research Letters*, 49(8), e2021GL097699.

Nicolis, C., Vannitsem, S. & Royer, J.F. (1995) Short-range predictability of the atmosphere: mechanisms for superexponential error growth. *Quarterly Journal of the Royal Meteorological Society*, 121(523), 705–722.

O'Reilly, C.H. & Czaja, A. (2015) The response of the Pacific storm track and atmospheric circulation to Kuroshio Extension variability. *Quarterly Journal of the Royal Meteorological Society*, 141(686), 52–66.

Palmer, T., Doblas-Reyes, F., Weisheimer, A. & Rodwell, M. (2008) Toward seamless prediction: calibration of climate change projections using seasonal forecasts. *Bulletin of the American Meteorological Society*, 89(4), 459–470.

Park, M., Johnson, N.C., Hwang, J. & Jia, L. (2024) A hybrid approach for skillful multiseasonal prediction of winter North Pacific blocking. *NPJ Climate and Atmospheric Science*, 7(1), 227.

Pelly, J.L. & Hoskins, B.J. (2003) A new perspective on blocking. *Journal of the Atmospheric Sciences*, 60(5), 743–755.

Plaut, G. & Vautard, R. (1994) Spells of low-frequency oscillations and weather regimes in the Northern Hemisphere. *Journal of Atmospheric Sciences*, 51(2), 210–236.

Qiu, B., Chen, S. & Schneider, N. (2017) Dynamical links between the decadal variability of the Oyashio and Kuroshio Extensions. *Journal of Climate*, 30(23), 9591–9605.

Rex, D. (1950) Blocking action in the middle Tellus 46A (1994), troposphere and its effect upon regional climate. I. an aerological study of blocking. *Tjellus*, 2, 196–211.

Schiemann, R., Athanasiadis, P., Barriopedro, D., Doblas-Reyes, F., Lohmann, K., Roberts, M.J. et al. (2020) Northern Hemisphere blocking simulation in current climate models: evaluating progress from the Climate Model Intercomparison Project Phase 5 to 6 and sensitivity to resolution. *Weather and Climate Dynamics*, 1(1), 277–292.

Schwierz, C., Croci-Maspoli, M. & Davies, H.C. (2004) Perspicacious Indicators of Atmospheric Blocking. *Geophysical Research Letters*, 31(6), 2003GL019341.

Steinfeld, D. (2020) *ConTrack - contour tracking*. GitHub. https://github.com/steidani/ConTrack

Tatebe, H. & Watanabe, M. (2018) *IPCC DDC: MIROC MIROC6 model output prepared for CMIP6 CMIP historical*. Hamburg: World Data Center for Climate (WDCC) at DKRZ .

Tatebe, H., Ogura, T., Nitta, T., Komuro, Y., Ogochi, K., Takemura, T. et al. (2019) Description and basic evaluation of simulated mean state, internal variability, and climate sensitivity in MIROC6. *Geoscientific Model Development*, 12(7), 2727–2765.

Thomas, C., Voulgarakis, A., Lim, G., Haigh, J. & Nowack, P. (2021) An unsupervised learning approach to identifying blocking events: the case of European summer. *Weather and Climate Dynamics* 2, 581–608.

Tibaldi, S. & Molteni, F. (1990) On the operational predictability of blocking. *Tellus. Series A, Dynamic Meteorology and Oceanography*, 42(3), 343–365.

Vannitsem, S. & Nicolis, C. (1997) Lyapunov vectors and error growth patterns in a T21L3 quasigeostrophic model. *Journal of the Atmospheric Sciences*, 54(2), 347–361.

Virtanen, P., Gommers, R., Oliphant, T.E., Haberland, M., Reddy, T., Cournapeau, D. et al. (2020) SciPy 1.0: fundamental algorithms for Scientific Computing in Python. *Nature Methods*, 17(3), 261–272.

Woollings, T., Barriopedro, D., Methven, J., Son, S.W., Martius, O., Harvey, B. et al. (2018) Blocking and its response to climate change. *Current Climate Change Reports*, 4, 287–300.

Xavier, A.K., Demaeyer, J. & Vannitsem, S. (2024) Variability and predictability of a reduced-order land–atmosphere coupled model. *Earth System Dynamics*, 15(4), 893–912.

Yiou, P. (2014) AnaWEGE: a weather generator based on analogues of atmospheric circulation. *Geoscientific Model Development*, 7(2), 531–543.

Yiou, P., Vautard, R., Naveau, P. & Cassou, C. (2007) Inconsistency between atmospheric dynamics and temperatures during the exceptional 2006/2007 fall/winter and recent warming in Europe. *Geophysical Research Letters*, 34(21): L21808. https://doi.org/10.1029/2007GL031981

SUPPORTING INFORMATION

Additional supporting information can be found online in the Supporting Information section at the end of this article.

How to cite this article: Xavier, A.K., Hamilton, O., Faranda, D. & Vannitsem, S. (2026) Predictability of North Pacific blocking events: Analogue-based analysis of historical MIROC6 simulations. *Quarterly Journal of the Royal Meteorological Society*, e70104. Available from: https://doi.org/10.1002/qj.70104

APPENDIX A. PREDICTABILITY ANALYSIS ($\alpha = 0.20$)

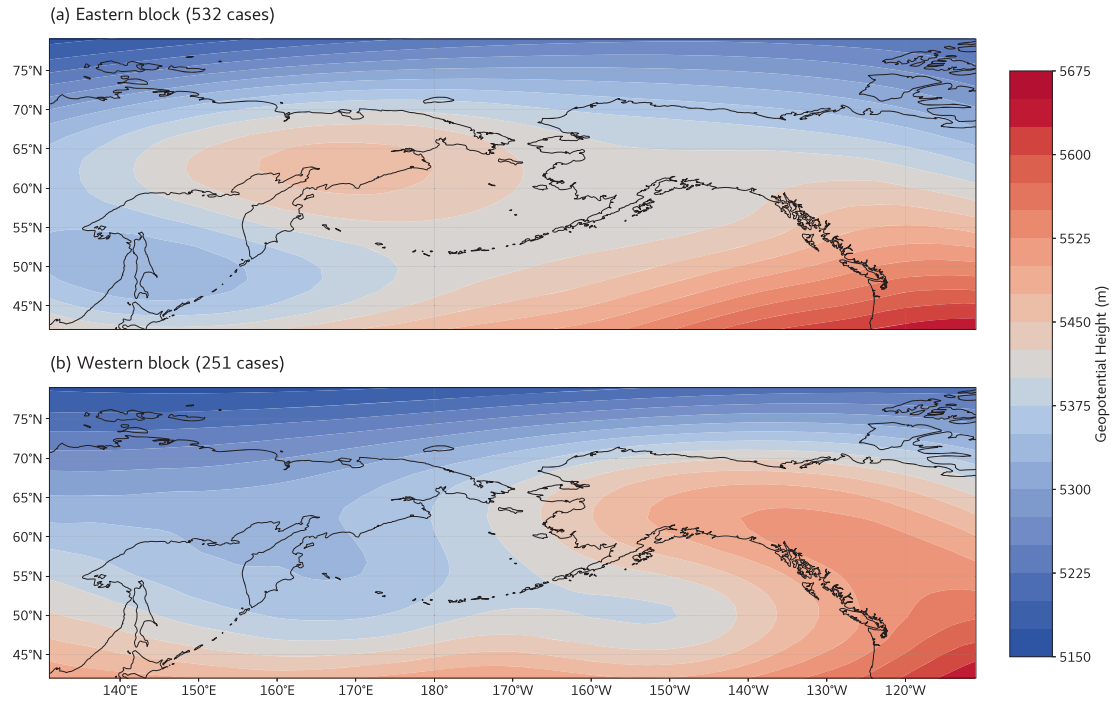

FIGURE A1 Same as Figure 3 with $\alpha = 0.20$. 532 eastern blocks and 251 western blocks are identified with this threshold. [Colour figure can be viewed at wileyonlinelibrary.com]

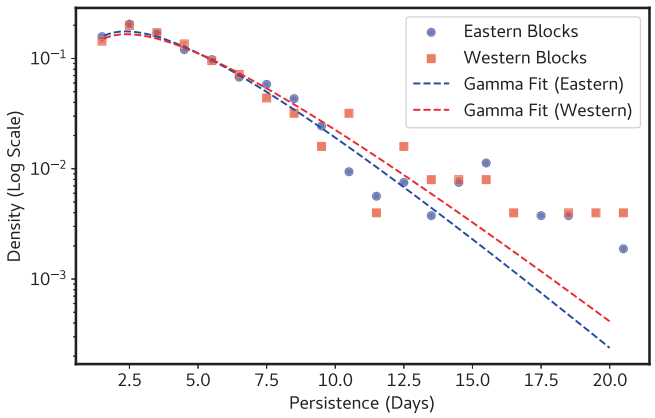

FIGURE A2 Same as Figure 4, but with $\alpha = 0.20$. [Colour figure can be viewed at wileyonlinelibrary.com]

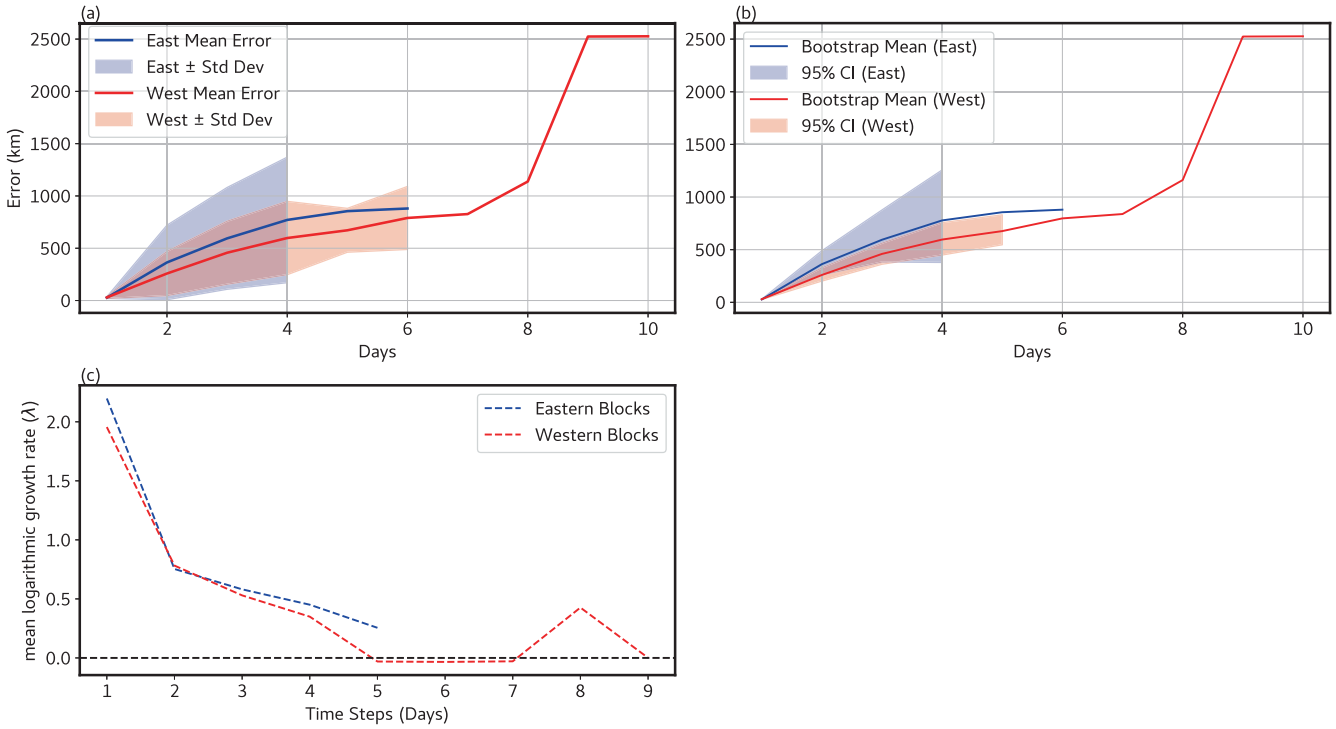

FIGURE A3 Same as Figure 6, but with $\alpha = 0.20$, considering the first 50 reference–analogue pairs. [Colour figure can be viewed at wileyonlinelibrary.com]

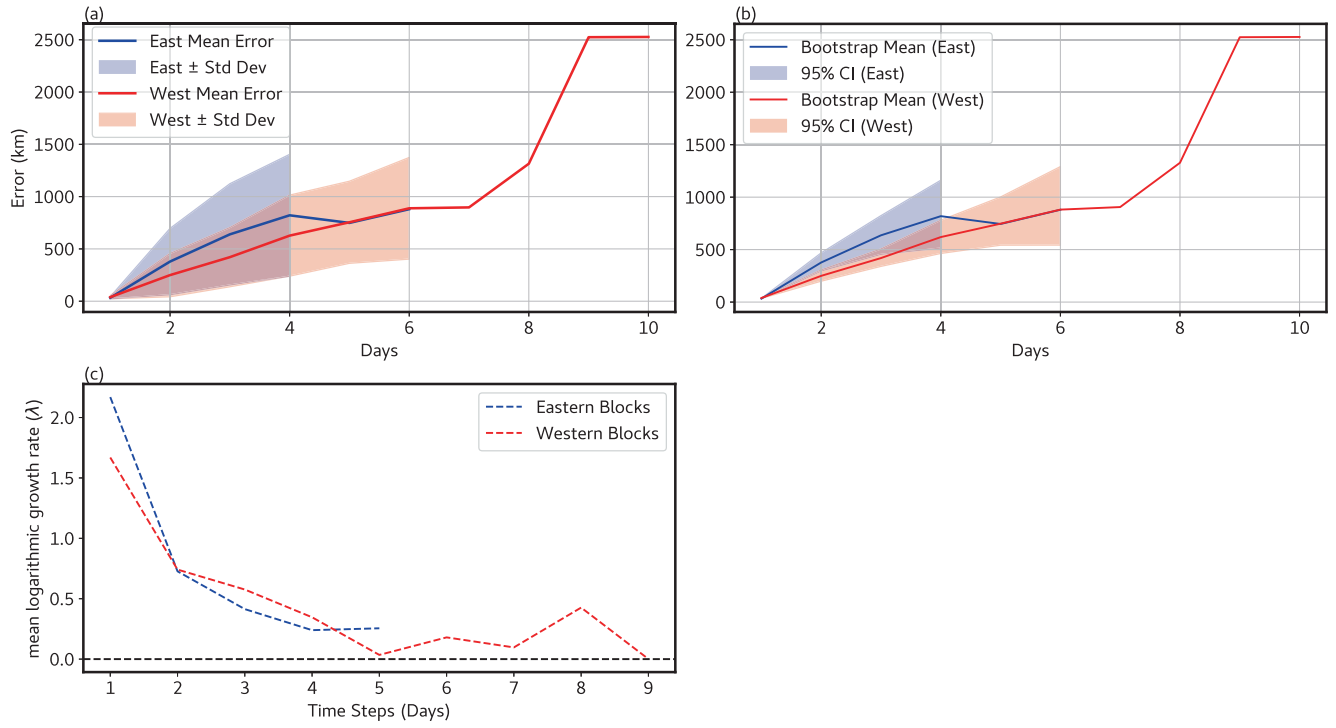

FIGURE A4 Same as Figure 6, but with $\alpha = 0.20$, considering the first 75 reference–analogue pairs. [Colour figure can be viewed at wileyonlinelibrary.com]